Effects of spatial resolution of the data on dynamic mode decomposition and its quantitative analysis

Jeonghoon Lee, Laurent Zimmer, Takeshi Saito, Shinji Nakaya, Mitsuhiro Tsue

Effects of spatial resolution of the data on dynamic mode decomposition and its quantitative analysis

Jeonghoon LEE[a], Laurent ZIMMER[b], Takeshi SAITO[c], Shinji NAKAYA[a], Mitsuhiro TSUE[a]

[a]*Department of Aeronautics and Astronautics, The University of Tokyo, 7-3-1, Hongo, Bunkyo, 113-8656, Tokyo, Japan*
[b]*Laboratoire EM2C, CNRS-CentraleSupélec-Université Paris Saclay, 3 rue Joliot-Curie, Gif-sur-Yvette, 91192, Cedex, France*
[c]*Dept. of Mechanical Engineering, Meisei University, 2-1-1, Hodokubo, Hino, 191-8506, Tokyo, Japan*

Abstract

Dynamic mode decomposition (DMD), based on Koopman analysis, is a tool capable of spatiotemporal analysis for various spatial resolutions, from one-dimensional signals to three-dimensional computational fluid dynamics (CFD) and experimental data. Outputs of the DMD consist of amplitudes, frequencies, decaying rates, and spatial modes. However, the effects of spatial resolution (time-series data in one-dimensional signal and spatial grid in two-dimensional data) and quantitative analysis of DMD are limited to one-dimensional signal data. In this study, the effects of spatial resolution with a fixed time scale of data and correction using scaling factors $2/\sqrt{A}$ on DMD amplitudes and $\sqrt{A}$ on DMD spatial mode strengths are investigated, where A is the number of the time-series data in one-dimensional signal or the number of the spatial grid in two-dimensional data. First, proofs of the scaling factors for one-dimensional(line layout) and two-dimensional(grid layout) data are presented. Second, the effect of spatial resolution on the amplitudes and spatial mode strengths and their scaled results are confirmed using one-dimensional artificial signal data, two-dimensional artificial signal field data, two-dimensional vortex shedding simulation data, and two-dimensional pulsating flow experimental data with various data resolutions. The results show that the amplitude increases proportionally with the spatial resolution, and the spatial mode strength is inversely proportional to the time series or spatial resolution of the data in all cases. As a result of applying the scaling factors to one-dimensional artificial signal and two-dimensional artificial

signal field data, the amplitudes and spatial modes contain the same values regardless of the change in spatial resolutions. The scaled amplitudes and spatial mode strengths on vortex shedding simulation and two-dimensional laminar pulsating jet show good agreements with slight differences, regardless of the spatial resolution change. The proposed scaling factor can be applied to compare data quantitatively obtained with different spatial resolutions.

Keywords: Dynamic mode decomposition, Spatial resolution, Scaling factor, DMD amplitudes, DMD spatial mode

---

1. Introduction

In fluid dynamics, many flow fields contain oscillations, instabilities, and spatially or temporally unsteady behaviors. Such phenomena can be understood through flow-field measurements. Various measurement methods such as pressure [1, 2], velocity [3, 4, 5, 6, 7], temperature [8, 9, 10], and chemiluminescence in the case of reacting systems [11, 12, 13] have been employed as effective diagnostics. The data acquired from these measurements have various sizes or grids, ranging from one-dimensional to three-dimensional shapes. Of course, there are various methods for analyzing these data.

The most common analysis tool is the Fast Fourier Transform (FFT). FFT is a standard processing approach for decomposing a signal into a series of waves at fixed frequencies and variable amplitudes. This method extracts the quantified amplitude regardless of the size of the initial data by multiplying it by $2/\sqrt{M}$, where M is the number of samples in the normalized unitary DFT[14]. However, FFT has some drawbacks. The output frequency basis of the FFT is fixed, meaning that the signal can only be decomposed into a uniform frequency basis, regardless of the dynamics of the signal. This basis is only linked to the number of samples and sampling frequency. Additionally, the FFT sampling rates must be within the Nyquist-Shannon criterion, implying that the sampling rates should be at least twice the targeted frequency.

Dynamic Mode Decomposition (DMD), presented by Schmidt[15] and Rowley[16], is a possible alternative for investigating dynamics in data of various dimensions. DMD is a method based on Koopman analysis of an infinite-dimensional linear operator[17]. Unlike FFT, DMD can extract dynamical characteristics such as frequencies, amplitudes, and decaying rates based on the Koopman operator [18]. Moreover, the frequency basis of DMD

is not fixed a priori but is computed for each data set. Unlike the overall number of points in the frequency domain, which is the same as in FFT, the spacing between those points is not regular, and the outputs are locked to the frequency of the targeted phenomena.

Although DMD exhibits these advantages, quantitative analysis on DMD amplitudes is limited. Most of the DMD results showed normalized amplitudes based on the maximum values of the results[19, 20, 21, 22]. Apart from this normalization approach, quantitative analysis was mainly conducted on one-dimensional time-series data by Kutz et al.[23], who compared the FFT power spectrum and DMD amplitude for 1-dimensional artificial signal data with fixed frequencies of 7 Hz (amplitude: 14) and 13 Hz (amplitude: 5). By applying a scaling factor of $2/\sqrt{M}$ (M: number of data points corresponding to one-dimensional time series data) to the power spectral density of the FFT and amplitudes of the DMD, quantitative analysis on DMD amplitudes was achieved in noise-free and noise-added one-dimensional time series data(for example, 50 or 100 points with dt = 0.01 second containing 7 Hz data were sampled). They showed that the data length strongly affects the DMD amplitudes and FFT power spectral density. However, only the scaling on DMD amplitudes for one-dimensional data has been discussed without any mathematical proof. A potential problem about the changes of spatial mode strength provided by the DMD is not addressed. Because data reconstruction in DMD is related to DMD amplitudes, spatial modes, and eigenvalues, which include information on frequencies and decay rates, spatial modes are also highly likely to be affected by changes in DMD amplitudes with respect to spatial grids. Additionally, it must be addressed whether these characteristics can be applied not only to projected DMD but also to other DMD methods (e.g., sparsity-promoting DMD)[24]. Therefore, it is necessary to clarify the effects of spatial resolution on DMD and the possibility of quantitative analysis. In many experiments, acquiring one-dimensional- or two-dimensional- or three-dimensional data with a consistent spatial resolution is very challenging. Furthermore, it may be difficult to perform simulations with the same number of meshes in computational fluid dynamics simulations because of limited computational resources. If DMD amplitudes and DMD spatial modes are normalized based on their respective maximum values, incorrect interpretations of the target flow field may occur due to excessive DMD amplitudes or DMD spatial mode strengths caused by external variables such as data noise. Thus, mathematical approaches for the quantitative analysis of DMD are required to understand the flow phenomena

accurately.

This study investigates the effects of spatial resolution (time-series data in one-dimensional signal and spatial grid in two-dimensional data) on the amplitudes and spatial mode strengths. It further aims to provide a quantitative analysis of DMD amplitudes and spatial mode strengths with properly defined scaling factors for amplitudes and spatial modes. First, analysis of two types of DMD analysis(projected DMD and sparsity-promoting DMD) will be implemented for one-dimensional artificial signals with various sizes of time-series data. The dominant amplitude and spatial mode with and without corrections will be compared. Additionally, the sparsity-promoting DMD(SPDMD) results are presented in this section. Then, time series two-dimensional artificial signal fields will be considered. The effects of grid sizes on amplitude and spatial mode in two-dimensional data and quantification methods will be investigated. Third, vortex-shedding calculated using Immersed Boundary Projection Method (IBPM) with various spatial grids will be considered. Unlike artificial signals, vortex shedding data contain a dominant mode and its harmonics. The effects of the scaling factors on amplitudes and spatial modes will be discussed. Finally, projected DMD analysis will be implemented on PIV experimental data with various interrogation windows. The changes in amplitudes and strength of spatial modes with various spatial grids will be depicted. Corrected amplitudes and strength of spatial modes will be compared with those obtained without correction.

2. Dynamic mode decomposition and scaling factors

2.1. Algorithm of dynamic mode decomposition

Dynamic Mode Decomposition (DMD), which is linked to the Koopman analysis as suggested by Rowley[16] and Schmid[25], is used to analyze the dynamics of the flows from the data sets. A brief Koopman and DMD analysis theory, as well as the computational procedure, is explained below. In a discrete-time dynamical system, the equation is written as:

$$\mathbf{x}_{k+1} = \mathbf{f}(\mathbf{x}_k), \tag{1}$$

where $\mathbf{x}_k = \mathbb{R}^n$ is a vector showing the state of the dynamical system at time step k. Koopman operator $\mathcal{K}$, an infinite-dimensional linear operator acting on the Hilbert space $\mathcal{H}$ of scalar observable functions g, maps g to a function $\mathcal{K}g$. Thus, the Koopman operator provides information on dynamical

systems as follows:

$$\mathcal{K}g(\mathbf{x}_k) = g(\mathbf{f}(\mathbf{x}_k)) = g(\mathbf{x}_{k+1}). \tag{2}$$

From eigendecomposition, the Koopman operator is decomposed:

$$\mathcal{K}\varphi_j(\mathbf{x}) = \lambda_j \varphi_j(\mathbf{x}) \qquad j = 1, 2, ..., \tag{3}$$

where $\varphi_j(\mathbf{x})$ are the Koopman eigenfunctions, which form the basis of expansion for the observables $\mathbf{g}(\mathbf{x}_k)$, and λ_j are the Koopman eigenvalues. In this analysis, the observables $\mathbf{g}$ are referred to in terms of the eigenfunctions:

$$\mathbf{g}(\mathbf{x}) = \sum_{j=1}^{\infty} \varphi_j(\mathbf{x}) \mathbf{v}_j, \tag{4}$$

where $\mathbf{v}_j$ is the Koopman modes that have the vector coefficients. From the definitions of Equation (3) and (4), the vector of observables $\mathbf{g}$ can be written as

$$\mathbf{g}(\mathbf{x}_k) = \sum_{j=1}^{\infty} \lambda_j^k \varphi_j(\mathbf{x}) \mathbf{v}_j, \tag{5}$$

where the Koopman eigenvalues λ_j contain information on the time evolution associated with the Koopman modes.

The DMD algorithm extracts the Koopman modes and Koopman eigenvalues directly. In the discrete observable matrices $\mathbf{X}(\mathbf{x}_1, \mathbf{x}_2, ..., \mathbf{x}_m)$ based on the data matrix, two slightly different data sets $\mathbf{X}_1(\mathbf{x}_1, \mathbf{x}_2, ..., \mathbf{x}_{m-1})$ and $\mathbf{X}_2(\mathbf{x}_2, \mathbf{x}_3, ..., \mathbf{x}_m)$ are taken. Then, one seeks the best-fit linear operator $\mathbf{A}$, taken with the Koopman operator:

$$\mathbf{A}\mathbf{X}_1 = \mathbf{X}_2. \tag{6}$$

The best-fit linear operator $\mathbf{A}$ is then computed using the pseudo-inverse of $\mathbf{X}_1$ and $\mathbf{X}_2$ as follows:

$$\mathbf{A} = \mathbf{X}_2 {\mathbf{X}_1}^{\dagger}. \tag{7}$$

Due to the large dimensions of the snapshot matrix $\mathbf{X}$, a Singular Value Decomposition (SVD) on $\mathbf{X}_1$ is applied to calculate the linear operator matrix $\mathbf{A}$:

$$\mathbf{A} = \mathbf{X}_2 \mathbf{V} \mathbf{\Sigma}^{-1} \mathbf{U}^*, \tag{8}$$

where $\mathbf{U}$, $\mathbf{V}$, and $\mathbf{\Sigma}$ are the left-singular vectors, right-singular vectors, and singular values of matrix $\mathbf{X}_1$, respectively. There is a more efficient method for finding the linear operator $\tilde{\mathbf{A}}$ using a projection of the full matrix $\mathbf{A}$ onto the POD modes:

$$\tilde{\mathbf{A}} = \mathbf{U}^* \mathbf{A} \mathbf{U} = \mathbf{U}^* \mathbf{X}_2 \mathbf{V} \mathbf{\Sigma}^{-1}. \tag{9}$$

By performing eigendecomposition on $\tilde{\mathbf{A}}$, eigenvalues and eigenvectors can be computed as follows:

$$\tilde{\mathbf{A}} \mathbf{W} = \mathbf{\Lambda} \mathbf{W}, \tag{10}$$

where the columns of $\mathbf{W}$ are the eigenvectors and $\mathbf{\Lambda}$ is a diagonal matrix with λ_k. The projected DMD modes are then computed using the following eigenvectors:

$$\mathbf{\Phi} = \mathbf{U} \mathbf{W}. \tag{11}$$

Frequencies f_j and growth or decaying rates σ_j are computed using λ_j:

$$f_j = \mathrm{Im}\left(\frac{log \lambda_j}{2\pi \Delta t}\right), \sigma_j = \mathrm{Re}\left(\frac{log \lambda_j}{\Delta t}\right). \tag{12}$$

Therefore, the initial amplitudes of each mode $\mathbf{b}$ are obtained by taking the pseudo-inverse of the DMD modes $\mathbf{\Phi}$ and the initial snapshot $\mathbf{x}_1$:

$$\mathbf{b} = \mathbf{\Phi}^{\dagger} \mathbf{x}_1. \tag{13}$$

Now, the observable data $\mathbf{x}(\mathbf{k})$ can be reconstructed using $\mathbf{\Phi}$, $\mathbf{\Lambda}$, and $\mathbf{b}$:

$$\mathbf{x}(\mathbf{k}) = \mathbf{\Phi} \mathbf{\Lambda}^k \mathbf{b}. \tag{14}$$

2.2. Scaling factor for DMD on one-dimensional sinusoidal data

In this study, we suggest two scaling factors for quantitative comparisons. One is for the amplitudes, and the other is for the spatial modes. Proof of these scaling factors is provided in this section. First, one-dimensional sinusoidal signals are considered. The signals can be described using Equation (15), as taken from several references[26, 27, 28] by setting the amplitude a_k, angular frequency w_k, damping factor α_k, and the initial phase ϕ_k with a k^{th} sinusoidal component, as follows:

$$\mathbf{x}(\mathbf{t}) = \sum_{k=1}^{K} a_k \exp\left((\alpha_k + i w_k) t + i \phi_k\right) = \sum_{k=1}^{K} c_k z_k^t, t = 1, 2, 3, 4, ..., M, \tag{15}$$

where $c_k = a_k \exp(i\phi_k)$ is the complex-valued k^{th} amplitude, and $z_k = \exp(\alpha_k + iw_k)$ is the k^{th} signal. To simplify Equation (15), no-damped signals with an initial phase of zero are considered. Equation (15) can therefore be rewritten as

$$\mathbf{x}(\mathbf{t}) = \sum_{k=1}^{K} a_k \exp((iw_k)t) = \sum_{k=1}^{K} a_k z_k^t, \tag{16}$$

where $z_k = \exp(iw_k)$. Thus, the time-shifted matrix of these signals, with $\mathbf{X} \in \mathbb{R}^{M \times N}$(where N represents the number of time-shifted values), can be expressed as shown in Equation (17):

$$\mathbf{X} = \begin{bmatrix} x_1 & x_2 & & x_N \\ x_2 & x_3 & \dots & x_{N+1} \\ & \vdots & \ddots & \vdots \\ x_M & x_{M+1} & \dots & x_{M+N-1} \end{bmatrix} = \sum_{k=1}^{K} a_k \begin{bmatrix} z_k & z_k^2 & & z_k^N \\ z_k^2 & z_k^3 & \dots & z_k^{N+1} \\ & \vdots & \ddots & \vdots \\ z_k^M & z_k^{M+1} & \dots & z_k^{M+N-1} \end{bmatrix}. \tag{17}$$

The time-shifted matrix $\mathbf{X}$ in Equation (17) is decomposed by SVD. The left singular vector and right singular vector are calculated by the eigenvalue decomposition of the covariance matrix and the Gram matrix of $\mathbf{X}$, respectively. In this section, only the calculation process of the left singular vector using the covariance matrix $\mathbf{R}$ in Equation (18) is given due to the similar process for calculating the right singular vector using the Gram matrix

$$\mathbf{R} = \mathbf{X}\mathbf{X}^* = \sum_{k=1}^{K} a_k \begin{bmatrix} z_k & z_k^2 & & z_k^N \\ z_k^2 & z_k^3 & \dots & z_k^{N+1} \\ & \vdots & \ddots & \vdots \\ z_k^M & z_k^{M+1} & \dots & z_k^{M+N-1} \end{bmatrix} \sum_{k=1}^{K} a_k \begin{bmatrix} z_k & z_k^2 & & z_k^N \\ z_k^2 & z_k^3 & \dots & z_k^{N+1} \\ & \vdots & \ddots & \vdots \\ z_k^M & z_k^{M+1} & \dots & z_k^{M+N-1} \end{bmatrix}^*$$

$$= \sum_{k=1}^{K} a_k \begin{bmatrix} z_k & z_k^2 & & z_k^N \\ z_k^2 & z_k^3 & \dots & z_k^{N+1} \\ & \vdots & \ddots & \vdots \\ z_k^M & z_k^{M+1} & \dots & z_k^{M+N-1} \end{bmatrix} \sum_{k=1}^{K} a_k \begin{bmatrix} z_k^{-1} & z_k^{-2} & & z_k^{-M} \\ z_k^{-2} & z_k^{-3} & \dots & z_k^{-(M+1)} \\ & \vdots & \ddots & \vdots \\ z_k^{-N} & z_k^{-(N+1)} & \dots & z_k^{-(M+N-1)} \end{bmatrix}$$

$$= N \sum_{k=1}^{K} a_k \sum_{k=1}^{K} a_k \begin{bmatrix} 1 & z_k^{-1} & & z_k^{(1-M)} \\ z_k^1 & 1 & \dots & z_k^{(2-M)} \\ & \vdots & \ddots & \vdots \\ z_k^{(M-1)} & z_k^{(M-2)} & \dots & 1 \end{bmatrix}. \quad (18)$$

Taking the eigenvalue decomposition of the covariance matrix $\mathbf{R}$ leads to the following:

$$\mathbf{R} = \mathbf{Q}\mathbf{\Lambda}\mathbf{Q}^* =$$

$$\begin{bmatrix} 1 & 1 & & 1 \\ z_1 & z_2 & \dots & z_K \\ & \vdots & \ddots & \vdots \\ z_1^{M-1} & z_2^{M-1} & \dots & z_K^{M-1} \end{bmatrix} \mathbf{\Lambda} \begin{bmatrix} 1 & z_1^{-1} & & z_1^{-(M-1)} \\ 1 & z_2^{-1} & \dots & z_2^{-(M-1)} \\ & \vdots & \ddots & \vdots \\ 1 & z_K^{-1} & \dots & z_K^{-(M-1)} \end{bmatrix} = \mathbf{U}\mathbf{\Lambda}\mathbf{U}^*, \quad (19)$$

where * denotes the conjugate transpose. The SVD of the time-shifted matrix $\mathbf{X}$ can be expressed as Equation (20) by taking the eigenvalue decomposition of the covariance matrix and the Gram matrix of $\mathbf{X}$:

$$\mathbf{X} = \mathbf{U}\mathbf{\Sigma}\mathbf{V}^*$$

$$= \begin{bmatrix} 1 & 1 & & 1 \\ z_1 & z_2 & \dots & z_K \\ & \vdots & \ddots & \vdots \\ z_1^{M-1} & z_2^{M-1} & \dots & z_K^{M-1} \end{bmatrix} \begin{bmatrix} c_1 & 0 & 0 & & 0 \\ 0 & c_2 & 0 & \dots & 0 \\ & \vdots & & \ddots & \vdots \\ 0 & 0 & 0 & \dots & c_K \end{bmatrix} \begin{bmatrix} 1 & z_1^{-1} & & z_1^{-(N-1)} \\ 1 & z_2^{-1} & \dots & z_2^{-(N-1)} \\ & \vdots & \ddots & \vdots \\ 1 & z_K^{-1} & \dots & z_K^{-(N-1)} \end{bmatrix}. \quad (20)$$

The left singular vector $\mathbf{U}$ and the right singular vector $\mathbf{V}$ are Vandermonde matrices. The shapes of these matrices are similar to those of a DFT matrix[14]. From Kuian et al.[29], $\mathbf{U}\mathbf{U}^* = K\mathbf{I}$ and $\mathbf{V}\mathbf{V}^* = K\mathbf{I}$ are established as well as $\mathbf{U}^*\mathbf{U} = M\mathbf{I}$ and $\mathbf{V}^*\mathbf{V} = N\mathbf{I}$. To satisfy a unitary matrix in each case, scaling factors $\frac{1}{\sqrt{M}}$ for $\mathbf{U}^*\mathbf{U} = M\mathbf{I}$, $\frac{1}{\sqrt{N}}$ for $\mathbf{V}^*\mathbf{V} = N\mathbf{I}$, and $\frac{1}{\sqrt{K}}$ for $\mathbf{U}\mathbf{U}^* = K\mathbf{I}$ and $\mathbf{V}\mathbf{V}^* = K\mathbf{I}$ should be applied.

Regarding the DMD on the 1-Dimensional time-shifted matrix, the amplitudes $\mathbf{b}$ of each mode are calculated as in Equation (21):

$$\mathbf{b} = \mathbf{\Phi^{-1}}\mathbf{x_1} = \mathbf{W^{-1}}\mathbf{U}^*\mathbf{x_1}. \tag{21}$$

where $\mathbf{U}^*$ denotes the conjugate transpose of the left-singular vectors of $\mathbf{X}_1$. Moreover, the amplitudes range from negative to positive frequencies, indicating that the amplitudes should be considered twice. Thus, the scaling factor $\frac{2}{\sqrt{M}}$ should be applied for the quantification of DMD amplitudes[23].

Next, spatial modes are considered. The original data can be approximated as shown in Equation (14). As the amplitudes are enlarged by $\sqrt{M}$, the strength of spatial modes will decrease. Therefore, $\sqrt{M}$ should be multiplied to extract spatial modes, excluding any changes caused by the number of sampled data.

2.3. Scaling factor for DMD analysis to two-dimensional signal field data

In this section, discrete-time two-dimensional sinusoidal wave image data are considered in the projected DMD analysis. The dimension of each image is $\mathbf{g} \in \mathbb{R}^{M\times N}$ taken at a discrete-time t, ranging from 1 to T. Values of the vertical axis of the image are assumed to follow the expression given below:

$$x(t) = \sum_{k=1}^{K} a_k \exp\left((iw_k)t\right) = \sum_{k=1}^{K} a_k z_k^t, t = 1, 2, 3, ..., T, \tag{22}$$

$$\mathbf{g_1} = \begin{bmatrix} x_1 & x_1 & & x_1 \\ x_2 & x_2 & \dots & x_2 \\ & \vdots & \ddots & \vdots \\ x_M & x_M & \dots & x_M \end{bmatrix}, \mathbf{g_2} = \begin{bmatrix} x_2 & x_2 & & x_2 \\ x_3 & x_3 & \dots & x_3 \\ & \vdots & \ddots & \vdots \\ x_{M+1} & x_{M+1} & \dots & x_{M+1} \end{bmatrix}$$

$$, ..., \mathbf{g_t} = \begin{bmatrix} x_t & x_t & & x_t \\ x_{t+1} & x_{t+1} & \dots & x_{t+1} \\ & \vdots & \ddots & \vdots \\ x_{M+t} & x_{M+t} & \dots & x_{M+t} \end{bmatrix}. \quad (23)$$

By vectorization of each image, the data matrix $\mathbf{G} \in \mathbb{R}^{(M \cdot N) \times T}$ can be rewritten as:

$$\mathbf{G} = (M \times N) rows \left\{ \underbrace{\begin{bmatrix} x_1 & x_2 & \dots & x_T \\ x_2 & x_3 & \dots & x_{T+1} \\ \vdots & \vdots & \ddots & \vdots \\ x_M & x_{M+1} & \dots & x_{M+T} \\ x_1 & x_2 & & x_T \\ x_2 & x_3 & \dots & x_{T+1} \\ \vdots & \vdots & \ddots & \vdots \\ x_M & x_{M+1} & & x_{M+T} \\ \vdots & \vdots & \ddots & \vdots \\ x_1 & x_2 & & x_T \\ x_2 & x_3 & \dots & x_{T+1} \\ \vdots & \vdots & \ddots & \vdots \\ x_M & x_{M+1} & \dots & x_{M+T} \end{bmatrix}}_{\text{T columns}} \right. = \sum_{k=1}^{K} a_k \begin{bmatrix} z_k & z_k^2 & & z_k^T \\ z_k^2 & z_k^3 & \dots & z_k^{T+1} \\ \vdots & \vdots & \ddots & \vdots \\ z_k^M & z_k^{M+1} & \dots & z_k^{M+T} \\ z_k & z_k^2 & & z_k^T \\ z_k^2 & z_k^3 & \dots & z_k^{T+1} \\ \vdots & \vdots & \ddots & \vdots \\ z_k^M & z_k^{M+1} & \dots & z_k^{M+T} \\ \vdots & \vdots & \ddots & \vdots \\ z_k & z_k^2 & & z_k^T \\ z_k^2 & z_k^3 & \dots & z_k^{T+1} \\ \vdots & \vdots & \ddots & \vdots \\ z_k^M & z_k^{M+1} & \dots & z_k^{M+T} \end{bmatrix}. \quad (24)$$

Using the same procedures as for Equation (17) and (18), the left singular vector and right singular vector are obtained as follows:

$$\mathbf{U} = \begin{bmatrix} 1 & 1 & & 1 \\ z_1 & z_2 & & z_K \\ z_1^2 & z_2^2 & \dots & z_K^2 \\ \vdots & \vdots & & \vdots \\ z_1^{M-1} & z_2^{M-1} & \dots & z_K^{M-1} \\ 1 & 1 & & 1 \\ z_1 & z_2 & & z_K \\ z_1^2 & z_2^2 & \dots & z_K^2 \\ \vdots & \vdots & & \vdots \\ z_1^{M-1} & z_2^{M-1} & \dots & z_K^{M-1} \\ & & & \\ \vdots & \vdots & & \vdots \\ 1 & 1 & & 1 \\ z_1 & z_2 & & z_K \\ z_1^2 & z_2^2 & \dots & z_K^2 \\ \vdots & \vdots & & \vdots \\ z_1^{M-1} & z_2^{M-1} & \dots & z_K^{M-1} \\ & & & \end{bmatrix}, \mathbf{V} = \begin{bmatrix} 1 & 1 & 1 & & 1 \\ z_1 & z_2 & z_3 & & z_K \\ z_1^2 & z_2^2 & z_3^2 & \dots & z_K^2 \\ \vdots & \vdots & \vdots & & \vdots \\ z_1^{T-1} & z_2^{T-1} & z_3^{T-1} & \dots & z_K^{T-1} \\ 1 & 1 & 1 & & 1 \\ z_1 & z_2 & z_3 & & z_K \\ z_1^2 & z_2^2 & z_3^2 & \dots & z_K^2 \\ \vdots & \vdots & \vdots & & \vdots \\ z_1^{T-1} & z_2^{T-1} & z_3^{T-1} & \dots & z_K^{T-1} \\ \vdots & \vdots & \vdots & & \vdots \\ 1 & 1 & 1 & & 1 \\ z_1 & z_2 & z_3 & & z_K \\ z_1^2 & z_2^2 & z_3^2 & \dots & z_K^2 \\ \vdots & \vdots & \vdots & & \vdots \\ z_1^{T-1} & z_2^{T-1} & z_3^{T-1} & \dots & z_K^{T-1} \end{bmatrix}. \tag{25}$$

The size of the row in the matrix is linked to the size of the initial image $(M \times N)$ for two-dimensional signals. The shapes of the two matrices are also the shape of the Vandermonde matrix, which means that scaling factor $\frac{1}{\sqrt{M \times N}}$ for $\mathbf{U}^* \mathbf{U} = (M \times N)\mathbf{I}$ should be considered. Regarding the amplitudes, the factor $\frac{2}{\sqrt{M \times N}}$ should be taken into account. Regarding spatial modes, the initial values should be multiplied by a factor $\sqrt{M \times N}$. The applicability of the scaling factors to these cases will be presented in Section 3.

3. Applying scaling factors to Dynamic mode decomposition

3.1. Effects of the spatial data size on projected dynamic mode decomposition and sparsity-promoting DMD with and without scaling in one-dimensional artificial signal data

To investigate the effects of spatial resolution(one-dimensional signal: the number of sampled data points, two-dimensional data: the number of spatial

grids) and the corrected DMD amplitudes and spatial mode strengths by scaling factors, one-dimensional artificial signal, two-dimensional artificial signal field, two-dimensional CFD, and two-dimensional PIV experimental data are considered. In this section, the amplitude and spatial mode of the projected DMD are presented. Additionally, sparsity-promoting DMD(SPDMD) suggested by Jovanovic et al.[24] is also tested. The SPDMD provides the number of modes to be retained based on the data and automatically determines the most appropriate model order for an accurate analysis. This adaptability makes it suitable for applications where the underlying dynamics may be complex or poorly understood. The SPDMD is designed to handle high-dimensional data sets efficiently. However, if one-dimensional artificial signals do not contain any noise, amplitudes in one-dimensional artificial signals are produced exactly regardless of the data length. Therefore, this section will treat both projected DMD and SPDMD. For SPDMD analysis, an open-source code provided on Jovanovic's homepage is used. The parameters for the alternating direction method of multipliers(ADMM) on SPDMD analysis are ρ(positive quadratic penalty parameter) =1.0, $\epsilon_{(prime)}$ = 0.000001, $\epsilon_{(dual)}$=0.0001, maximum iteration = 10000 which are the initial values in Jovanovic's code. The SPDMD amplitudes are selected from the absolute value of the 'xpol' data in the answer variable in Jovanovic's code, representing the optimal amplitude obtained through the sparsity-promoting process.

To begin with, a signal with a single frequency of 10 Hz as used in Equation (26) is investigated in this section. Time t ranges from 0 seconds to 1.00 seconds with a 0.01 seconds interval($\Delta t = 0.01$ seconds).

$$x_t = Re(15 \times \exp(10 \times 2 \times \pi t \times i)). \tag{26}$$

Tu[30] and Tu et al.[31] mentioned that in order to perform DMD on a 1-dimensional signal, time-shifted matrix with at least three rows such as $\mathbf{X} = [\mathbf{X}(t) \quad \mathbf{X}(t+\Delta t) \quad \mathbf{X}(t+2\Delta t)]$ must be taken, where $\mathbf{X}(t)$ in matrix $\mathbf{X}$ means $[x_t \quad x_{t+\Delta t} \quad ...]^T$. This study also takes a time-shifted matrix so that $\mathbf{X_1} = [\mathbf{X}(t) \quad \mathbf{X}(t+\Delta t)]$ and $\mathbf{X_2} = [\mathbf{X}(t+\Delta t) \quad \mathbf{X}(t+2\Delta t)]$ are obtained. The length of data set $\mathbf{X}(t)$ varies from 2(0 s to 0.01 s) to 99(0 s to 0.98 s). A typical sample of the signal of the data sets is presented in Fig. 1 and in Equation (27) and (28). The rank for the SVD used in the DMD and the dimension of the data set in this analysis are two and $\mathbf{X} \in \mathbb{R}^{2 \sim 99 \times 3}$, respectively:

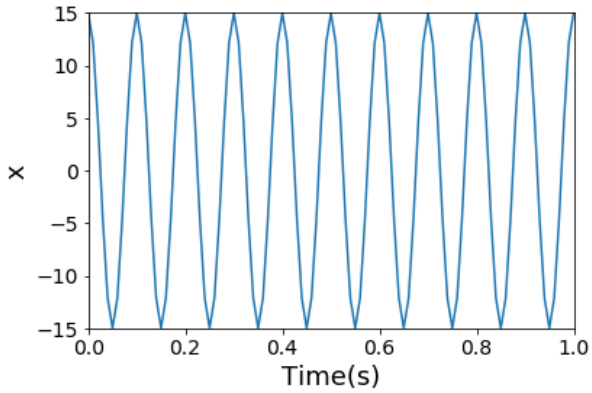

Figure 1: Signal plot from Equation (26).

$$\begin{bmatrix} | & | & | \\ \mathbf{X}(t) & \mathbf{X}(t+\Delta t) & \mathbf{X}(t+2\Delta t) \\ | & | & | \end{bmatrix} = \begin{bmatrix} x_0 & x_{0.01} & x_{0.02} \\ x_{0.01} & x_{0.02} & x_{0.03} \end{bmatrix} at\, \mathbf{X}_{length} = 2, \tag{27}$$

$$\begin{bmatrix} | & | & | \\ \mathbf{X}(t) & \mathbf{X}(t+\Delta t) & \mathbf{X}(t+2\Delta t) \\ | & | & | \end{bmatrix} = \begin{bmatrix} x_0 & x_{0.01} & x_{0.02} \\ x_{0.01} & x_{0.02} & x_{0.03} \\ \vdots & \vdots & \vdots \\ x_{0.98} & x_{0.99} & x_{1.00} \end{bmatrix} at\, \mathbf{X}_{length} = 99. \tag{28}$$

Fig. 2 shows the projected DMD and SPDMD amplitudes at the dominant mode with and without applying the scaling factor for various data lengths. The frequency of these amplitudes is precisely 10 Hz in all cases. It should be noted that the dominant mode is extracted successfully even though the data length is less than 10, even though this does not correspond to a complete cycle. Without applying the scaling factor, the amplitude shows an increasing tendency in both DMD algorithms. Interestingly, the amplitude is smaller than the original amplitude for cases corresponding to the length of the data set $\mathbf{X}$ below 4. At the data length of 4, the amplitude is 15 as the imposed amplitude since the value of the scaling factor is $1\,(2/\sqrt{(}4) = 1)$ for this length. When the data lengths are greater than 4,

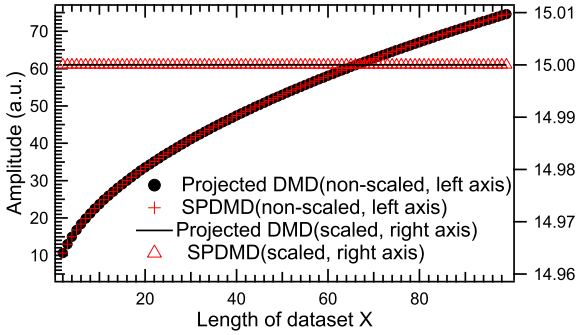

Figure 2: Dominant amplitude extracted by projected DMD and SPDMD with and without applying the scaling factor at various data lengths.

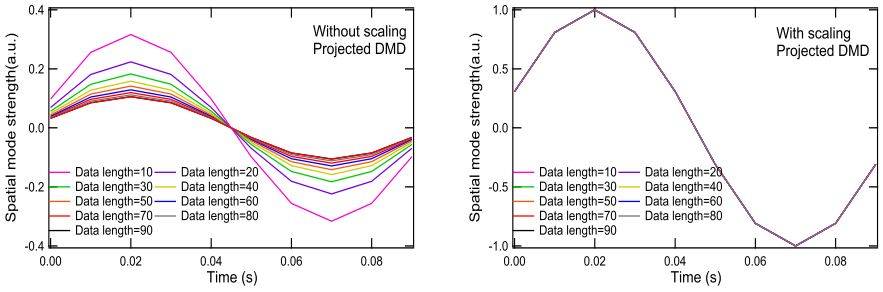

(a) (b)

Figure 3: Non-scaled(left) and scaled(right) dominant spatial mode of projected DMD at various data lengths.

the amplitude is higher than the imposed amplitude. These results imply that the DMD amplitudes are affected by the use of $\mathbf{U}^*$, which is a Vandermorde matrix with a shape similar to the DFT matrix. On the other hand, when the scaling factor is applied, amplitudes remain consistent in both the projected DMD and SPDMD, regardless of the length of the data set.

As presented in Section 2.2, the projected DMD modes are also influenced by the size of the time-series data. Fig. 3 presents the results of a scaled spatial mode and a non-scaled spatial mode for the projected DMD. The spatial mode of the SPDMD is not considered in this section because the target of the SPDMD is only the amplitudes. Fig. 3 (a) demonstrates that smaller time-series data lead to higher spatial mode strength without scaling. By applying the scaling factor, the spatial mode strength aligns perfectly, regardless of the data length, as depicted in Fig. 3 (b). These results indicate that scaling factors enable the quantitative interpretation of one-dimensional signal data.

3.2. Applying the scaling factors to projected DMD amplitude and spatial mode in a two-dimensional artificial signal field

The scaling factors successfully corrected the amplitude and spatial mode strength for one-dimensional signal data. However, most targets of DMD analysis are two-dimensional data. In this section, the focus is made on two-dimensional data to investigate the effects of spatial data size and the potential applications of the scaling factors. Unlike Section 3.1, only the projected DMD results are discussed from this section onwards. Two-dimensional signal data with various spatial resolutions used in this section are shown in Fig. 4. Four different spatial resolutions are used: 25×25(625 pixels), 50×50(2500 pixels), 75×75(5625 pixels), and 100×100(10000 pixels). The imposed signal is given in Equation (26). The time interval between the images is set to 0.01 s. A total of 101 images, representing a time series from 0 to 1 s, is used in all samples. The rank of SVD used in the DMD is set to two.

Fig. 5 shows the DMD mode amplitude at a dominant frequency of 10 Hz with and without applying the scaling factor. The dominant frequency for all spatial resolutions is 10 Hz. The uncorrected amplitude at the dominant frequency is 187.5 at 625 data points, 375 at 2500 data points, 562.5 at 5625 data points, and 750 at 10000 data points, far from the imposed amplitude. Meanwhile, after applying the scaling factor to the amplitude, the results show a constant value of 15. These results are the same as those obtained in Section 3.1.

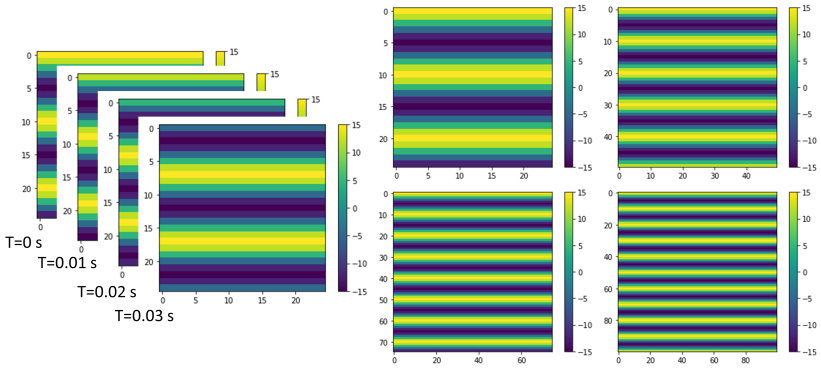

Figure 4: Images of two-dimensional data used in this section at various spatial resolutions(25x25, 50x50, 75x75, 100x100).

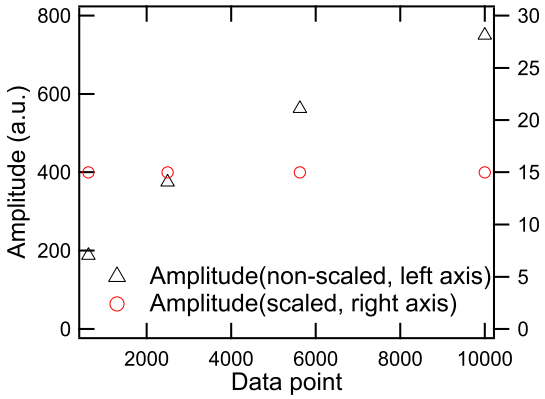

Figure 5: Mode amplitude at the dominant frequency of 10 Hz with(right axis) and without(left axis) applying the scaling factor.

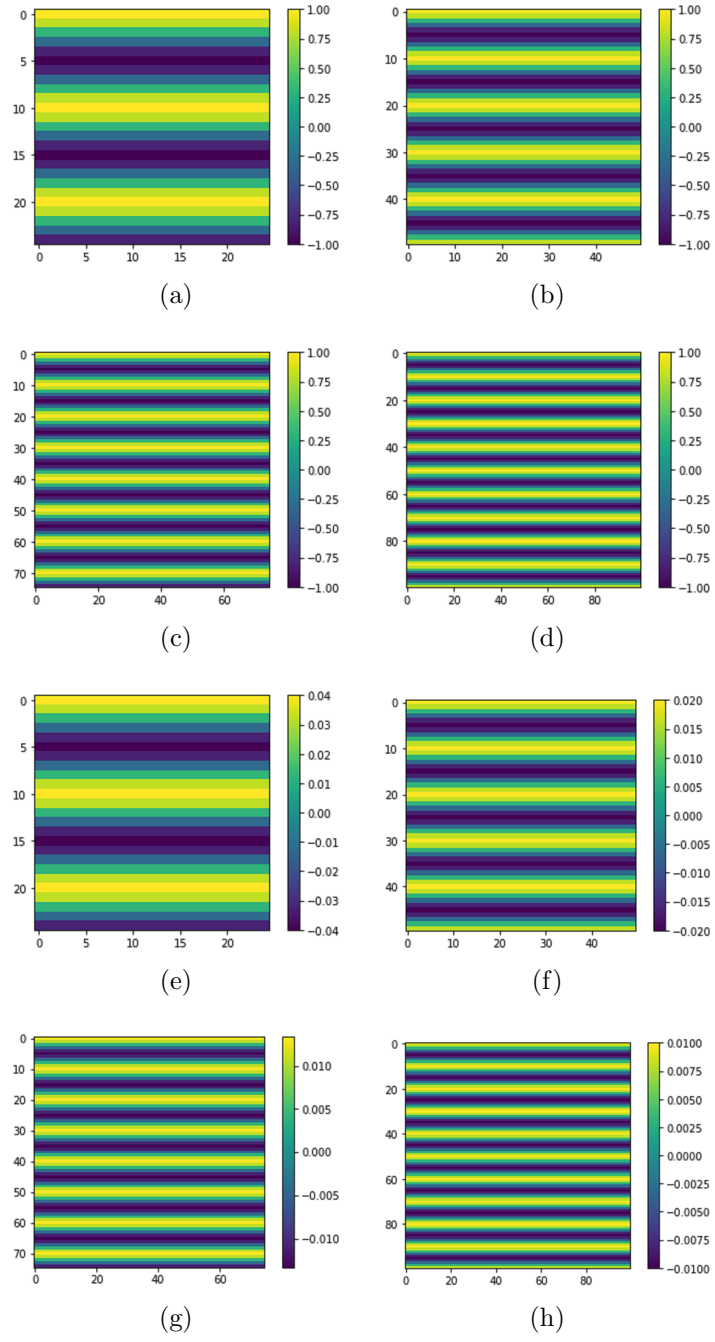

Figure 6: Spatial mode at the dominant frequency with (a-d) and without (e-h) scaling factor at different spatial resolutions.

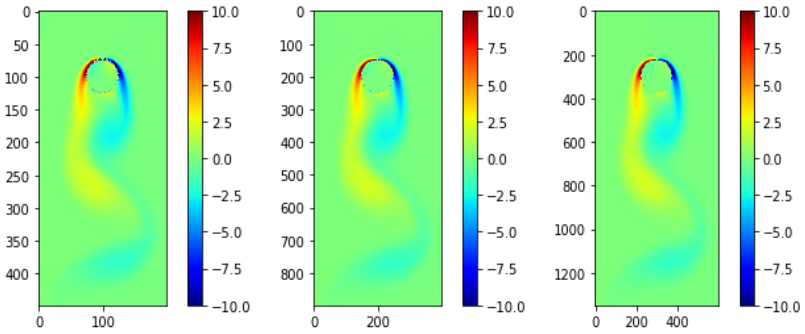

Figure 7: Sample vorticity images of vortex shedding simulated by IBPM at various spatial resolutions((a): 449x199, (b): 899x399, (c): 1349x599).

The spatial mode at the dominant frequency with and without applying the scaling factor at various spatial resolutions is depicted in Fig. 6. Without the scaling factor, the maximum and the minimum values of the dominant mode are ± 0.04 at 25×25 spatial resolution, ± 0.02 at 50×50 spatial resolution, ± 0.0133 at 75×75 spatial resolution, and ± 0.01 at 100×100 spatial resolutions, respectively. The strength of the mode decreases with increasing spatial resolution, indicating the data points also affect the strength of the mode. With the scaling factor, the maximum and minimum strength in the spatial mode remained at ± 1.

3.3. Effects of the spatial resolution and quantitative analysis of DMD using two-dimensional vortex shedding

The DMD results on one and two-dimensional artificial signal data with the proposed scaling factors give the possibilities for quantitative analysis. However, actual phenomena are not represented by such simple dynamical systems. Many phenomena, such as vortex shedding, pulsating flow, and jet-in-crossflow, are accompanied by dominant phenomena and their harmonics. In this section, numerical simulations of vortex shedding are performed with various spatial resolutions using an Immersed Boundary Projection Method (IBPM) as suggested by Colonius et al.[32]. DMD analysis is conducted on the simulated data to compare amplitudes and spatial modes with and without the scaling factors. Unlike in Sections 3.1 and 3.2, both dominant phenomena and harmonics will be considered.

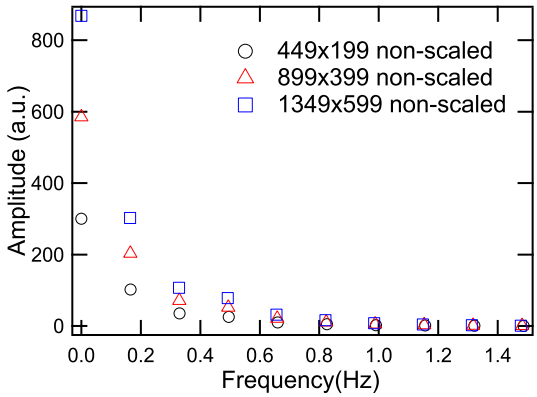

Figure 8: Non-scaled DMD power spectra on vortex shedding at various spatial resolutions.

Two-dimensional vortex shedding is simulated with various spatial resolutions. The grid of the flow field is set with spatial resolutions of 449×199, 899×399, and 1349×599, respectively. The length of the domain and diameter of the cylinder is 9×4 and 1, respectively. The lengths have been non-dimensionalized with respect to the cylinder diameter. We set 50, 100, and 150 points per cylinder diameter with multi-domain levels 4, 5, and 6 at a mesh of 449×199, 899×399, and 1349×599 so that the finest grid covers a domain of 9×4. The Reynolds number is set to 100 to remain in the laminar vortex shedding regime [33]. The time step Δt is 0.01, satisfying the CFL condition in all simulation grids[34]. In this study, the vorticity distribution is the target of DMD analysis as it most likely represents the main characteristics of vortex-shedding structures. Examples of the vorticity data calculated under these conditions are presented in Fig. 7. DMD analysis is conducted with three conditions. One thousand snapshots with regular intervals of $10\Delta t$ are taken. The rank is considered to be 20, capturing the information of harmonic oscillations. It should be noted that there may be slight differences in frequencies and amplitudes between each simulation result due to slightly different analysis conditions.

Fig. 8 and 9 show the DMD power spectra with and without applying the scaling factor. The amplitudes of the dominant mode and harmonics appear clearly. The detailed values are listed in Table 1. The non-scaled amplitudes are more than 2 times (at 899×399 spatial resolution) and 3 times (at 1349×599 spatial resolution) greater than the amplitudes at the 449×199 spatial resolution. The amplitude around 0.33Hz, the first harmonics of the

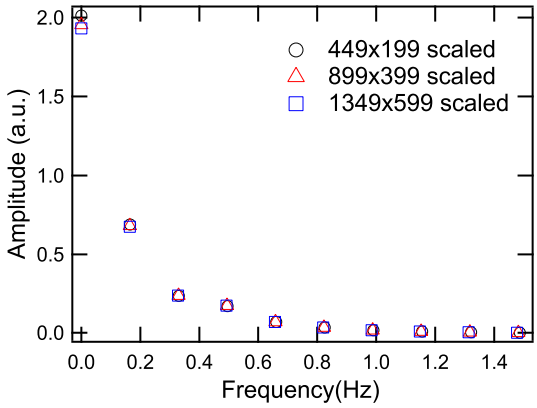

Figure 9: Scaled DMD power spectra on vortex shedding at various spatial resolutions.

Table 1: Amplitudes and frequencies of dominant mode and harmonics with and without scaling at various spatial resolutions.

spatial Resolution	Frequency(Hz)	Amplitude(a.u.)	
		Non-Scaled	Scaled
449×199	0.165(Dominant mode)	102.90	0.690
	0.330(First Harmonics)	35.45	0.237
	0.495(Second Harmonics)	25.49	0.172
899×399	0.165(Dominant mode)	203.37	0.681
	0.329(First Harmonics)	71.44	0.239
	0.494(Second Harmonics)	52.16	0.175
1349×599	0.164(Dominant mode)	302.70	0.674
	0.328(First Harmonics)	107.26	0.239
	0.492(Second Harmonics)	78.30	0.175

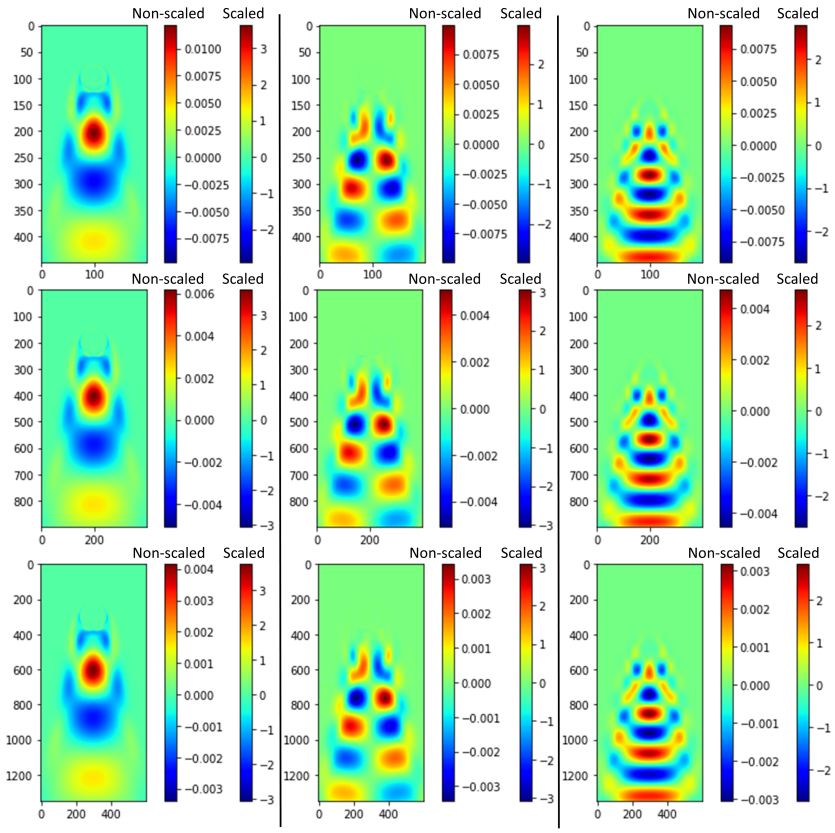

Figure 10: Spatial mode with and without scaling (left: dominant mode, center: first harmonics, right: second harmonics).

dominant mode, shows the same trend as in the case of 0.165 Hz. This trend can be explained by considering the square root of the number of data points 89 351 (449×199), 358 701 (899×399), and 805 655 (1349×599). The square roots of these values are 298.916, 598.917, and 897.583, showing differences of about 2 and 3 times bigger than 298.916. In contrast, the scaled amplitudes take similar values as shown in Fig. 9 and Table 1. The scaled amplitudes at the dominant frequency of 0.165 Hz are almost identical. The other amplitudes of the harmonics oscillations also have similar values, regardless of the spatial resolution.

Fig. 10 presents the dominant and secondary modes with and without scaling. There are two color bars in the figure, the left side shows the result without scaling, and the right side shows the result with scaling. The shapes of these modes are similar to those presented by Kutz et al. [23], Hemati et al.[35], and Noack et al.[36]. The strongest fluctuations appear at 0.165 Hz (corresponding to the dominant mode). For the secondary modes, the fluctuations are weakened compared to the dominant mode. As the spatial resolution increases, the strength of the dominant mode and its harmonics becomes smaller. This change is the same as that in the results shown in sections 3.1 and 3.2. On the other hand, the strengths in the dominant and secondary modes with the scaling factor are consistent regardless of the spatial resolutions. One should be noted that only the strength of the 449×199 case tends to have slightly smaller maximum and minimum values. The differences between these results may be due to the different simulation conditions.

3.4. DMD analysis on PIV experimental data

The results in Subsection 3.3 presented the effects of the various spatial data sizes on DMD amplitudes and spatial modes. In two-dimensional vortex shedding data, not only the amplitudes and spatial mode strengths on dominant modes but also the amplitudes and spatial mode strengths on harmonics of the DMD are strongly affected by spatial data sizes. Based on these results, this section investigates the effects of spatial resolutions in PIV data with different interrogation windows.

3.4.1. Experimental setup

The experimental setup used in this section is shown in Fig. 11. It is based on an atmospheric injection system with a co-flow configuration. The inner diameter is 20 mm, with a lip of 1 mm, and the outer diameter is 39

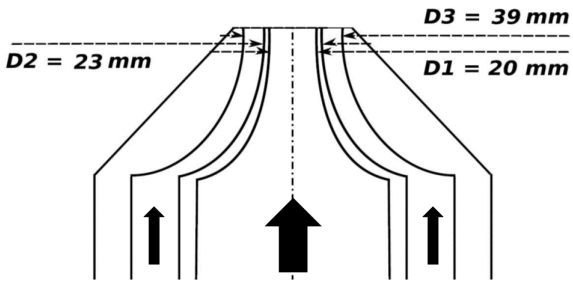

Figure 11: Schematic representation of the experimental setup(Black arrows meaning the direction of flow).

mm. The flow rate of the inner flow is 19.82 L/min, controlled by a Mass flow Controller (F-201-AV-50K-AAD-33-V Bronkhorst, and a maximum capacity of about 460 l/min at 1 bar,± 0.5% of reading states error). This main flow is modulated by a Direct Drive Valve (DDV) system (Moog) and leads to a mean convection velocity of 1.2 m/s, producing a laminar flow with a Reynolds number of about 1710. The flow rate of the outer part is 49.15 L/min controlled by a Mass flow Controller (F-201-AV-50K-AAD-33-V Bronkhorst and a maximum capacity of about 25 m^3/h at 1 bar ± 0.5% of reading states error). The signal imposed on the DDV system in this study is an 80 Hz sinusoidal function with an amplitude of 5 V and an offset of 2.5 V. The valve is closed at a voltage of 0 V or below, leading to strong oscillations in the current case. This frequency and signal generation have been chosen to generate large vortices. The modulation imposed on the main flow is controlled and acquired using a Labview program. The captured images are processed using Dantec Dynamic Studio with various interrogation windows. An adaptive correlation is performed in all cases with an initial window of 128×128. Tiny oil droplets (vacuum pump Edwards oil n°15) are added to the air through a nebulizer system to measure the velocity of the flow. Those droplets, with typical diameters of 1 or 2 µm [37], have a Stokes number small enough to represent the airflow faithfully.

3.4.2. DMD results on PIV data with various interrogation windows

A sample image of the droplets is presented in Fig. 12. These seeding droplets are continuously injected through the primary airflow system and the outer flow with a similar density. No seeding droplets are introduced in the air at rest around the outer flow, as the main interest of this research

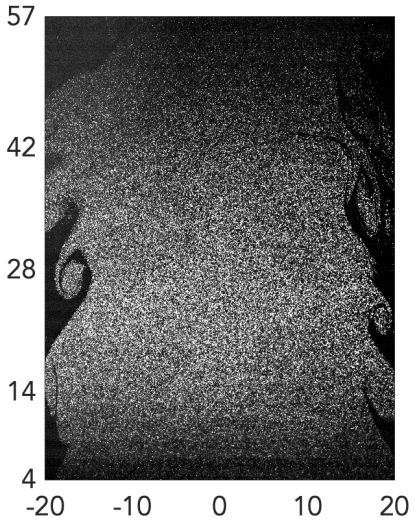

Figure 12: Sample image of Mie scattering image

is the description of the inner shear layer and the quantitative analysis of the vortices. The illumination of the droplets is achieved with a pulsed Nd: YAG laser (Edgewave, Innoslab) working at 5 kHz, with a pulse duration of 7 ns and a typical pulse intensity of 10 mJ at a wavelength of 532 nm. The laser beam is shaped into a planar sheet with a height of 50 mm and thickness of 1 mm at the measurement position. To record the images, a high-speed camera (Photron-FastCam with a spatial resolution of 1024 $\times$ 1024 pixels and working at 5 kHz) is used together with an objective of 105 mm (aperture of f#5.6) and an extension ring of 20 mm for magnifying the field of the interest. This imaging system is placed at 90° from the laser sheet to encompass a physical field of view of 68.2 mm$\times$68.2 mm. The exposure time is set to 5 µs. The total number of seeding particles in one image is about 19 000 particles/image, using simple software to count the particles per image. This result leads to approximately 9 particles/16$\times$16 pixels, except for the dark region in the image, corresponding to the ambient airflow. As seeding particles are introduced inside the two jets, velocity data at the shear layer between the pulsed stream and the outer stream are well captured.

An example of the instantaneous vector field and Y-axis velocity profile using 5 000 images in the 16$\times$16 interrogation window is presented in Fig.

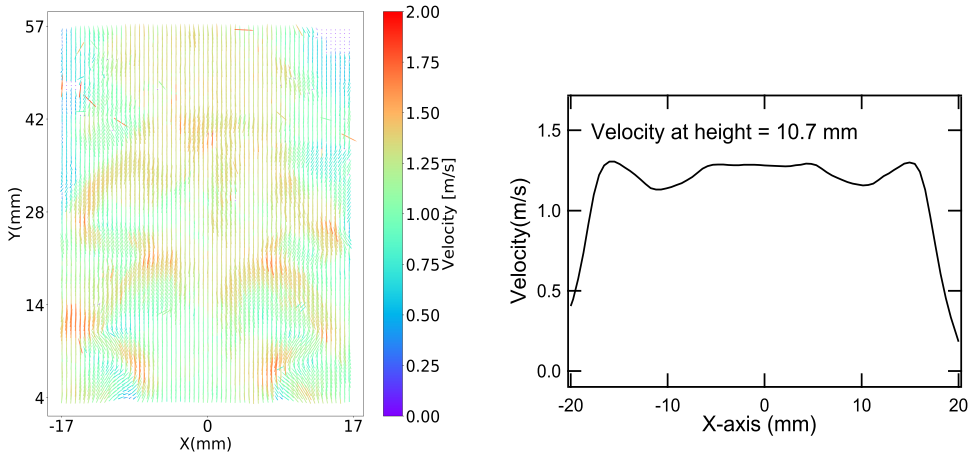

(a) (b)

Figure 13: Measured velocity with a 16×16 interrogation window. ((a) Vector field, (b) Averaged Y-axis velocity at the height of 10.7mm based on 5000 samples.)

13. Although four interrogation window conditions (16×16, 32×32, 48×48, 64×64) are used in this study, only the 16×16 case is presented as sample data due to the finest spatial resolution to observe the velocity profile. Fig. 13 (a) shows a typical velocity field used in this study. The analyzed vector field clearly shows the vortices at the left and right sides of the jet. The 80 Hz pulsating flow induces these vortices. The vertical velocity profile shown in Fig. 13 (b) is obtained at the height of 10.7 mm from the exit of the jet. The velocity profile is averaged over 5 000 consecutive velocity fields. The maximum velocity is about 1.2 m/s at the center of the jet. Slight velocity changes are observed on average between the two flows. The lower velocity at a radius of 10 mm corresponds to the influence of the inner lip, separating the two jets. The main region of interest in the current study is the inner shear layer between the inner and outer jet, and therefore, vortices located at around 10 mm (corresponding to half of the diameter) will be of interest.

To reduce the weight of the matrices in DMD analysis, horizontal velocity is used in the following section. This choice is motivated by the significant changes near the vortices. The unresolved velocity corresponding to the dark regions (left and right sides of the outer jet) is removed in the DMD computations. Twenty-seven data sets, each with 250 images per case, are used for extracting the dominant phenomena and the harmonics. The DMD power spectra for the four interrogation windows are presented in Fig. 14. The dis-

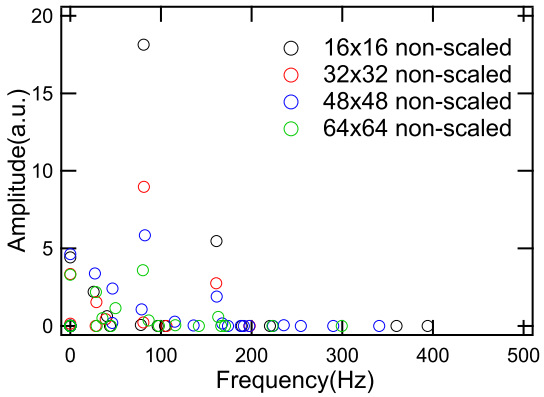

Figure 14: Non-scaled DMD power spectra on pulsating flow on one case with various spatial resolutions

played power spectra correspond to only one data set out of the twenty-seven computed. The spectra show that the 80 Hz dominant mode and its harmonics at 160 Hz appear clearly with the four interrogation windows. Unlike the results in Section 3.3, other harmonics are not observed in the current analysis. This may be due to noises or lower spatial resolutions of the PIV data compared to numerical data.

The DMD amplitudes at the dominant mode and its first harmonics on various interrogation windows are given in Fig. 15. The amplitudes and frequencies in this figure are averaged over the twenty-seven data sets. The results show that the 16×16 case leads to the highest DMD amplitude. With a reduction in spatial resolution, amplitudes become smaller. These results are consistent with those in section 3.3. Significant differences in standard deviations of amplitudes and frequencies between spatial resolutions are not seen. Fig. 16 represents the scaled power spectral diagram based on the PIV data with various spatial resolutions. The results show that amplitudes are around 0.4 at the dominant mode and 0.1 at the first harmonics. With an increased spatial resolution, the amplitude at the dominant frequency takes higher values. This result implies that data resolution may affect the accurate analysis of the flow field. A finer spatial resolution provides a better description of the vortices without being affected by noise. The detailed values on the dominant mode and harmonics are given in Table 2.

The effects of spatial resolution are also evident in the spatial mode strengths. Fig. 17 presents the scaled and non-scaled spatial modes for

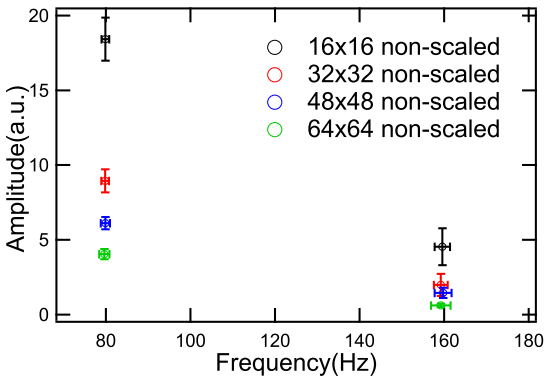

Figure 15: Amplitudes at the dominant mode and its first harmonics analyzed by DMD without scaling factor.

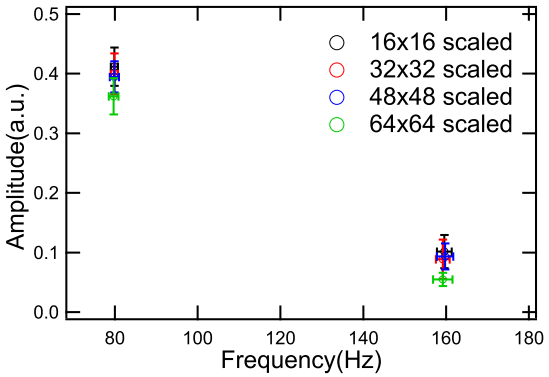

Figure 16: Amplitudes at the dominant mode and its first harmonics analyzed by DMD with the scaling factor.

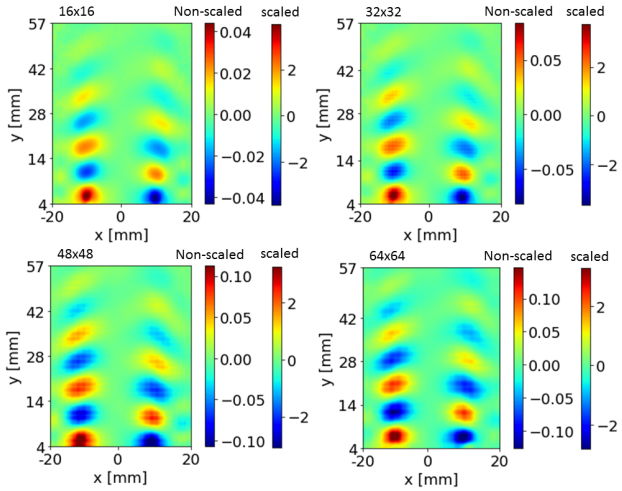

(a)

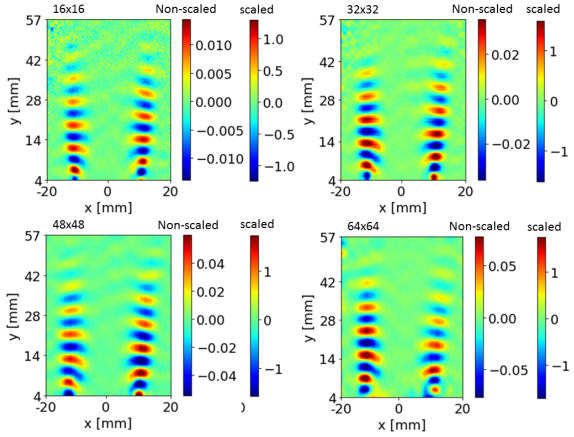

(b)

Figure 17: Average of spatial modes at the dominant frequency on various processing technique conditions (a) 80 Hz dominant mode for windows of 16, 32, 48, and 64 from left to right and top to bottom, (b) 160 Hz first harmonics for windows of 16, 32, 48 and 64 from left to right and top to bottom.

Table 2: Amplitudes and frequencies at dominant mode and its first harmonics with and without scaling for various interrogation windows.

Interrogation	Frequency(Hz)	Spatial strength(a.u.)	
		Non-scaled	Scaled
16×16	79.86(Dominant mode)	18.41	0.412
	159.57(First Harmonics)	4.548	0.102
32×32	79.85(Dominant mode)	8.940	0.400
	159.24(First Harmonics)	1.982	0.0886
48×48	79.89(Dominant mode)	6.117	0.395
	159.75(First Harmonics)	1.451	0.0936
64×64	79.66(Dominant mode)	4.048	0.362
	159.18(First Harmonics)	0.6137	0.0549

the dominant mode and its first harmonics across various resolutions. The left and right color bars in the figure represent the non-scaled strength and scaled strength, respectively.

The absolute values of maximum and minimum values of the spatial mode without scaling are proportional to the spatial resolution. This tendency is already observed in Section 3.3. Meanwhile, regardless of the spatial resolution, the scaled results have a similar value.

It is possible to compute the convection velocity of the structure by looking at the spatial mode. Taking the spacing between two consecutive maximums in a vertical line and a time corresponding to the inverse of the frequency associated with the peak of the DMD spectra ($1/80 = 12.5$ms), one retrieves a typical velocity of 1.2 ± 0.05 m/s for all cases, regardless of the spatial resolution.

4. Conclusions

This study investigates the effect of spatial data resolution(time-series data in one-dimensional signal and spatial grid in two-dimensional data) on the amplitudes and spatial mode strengths of DMD and its calibration method. From the mathematical proofs of the one-dimensional and two-dimensional data, the proposed scaling factors are $2/\sqrt{A}$ for the amplitudes

and $\sqrt{A}$ for the spatial mode strengths, where A corresponds to the number of points of time-series data in one-dimensional signal and spatial grid in two-dimensional data. Proofs of scaling factors for amplitudes and spatial modes are provided for one- and two-dimensional data using the projected DMD and sparsity-promoting DMD.

First, projected DMD and SPDMD analysis are performed on various lengths of one-dimensional artificial signal data. The results show that the amplitude at the dominant frequency increases with the factor of $\sqrt{A}/2$ in both DMD algorithms. This finding implies that the amplitudes of the DMD are affected by the use of $\mathbf{U}^*$, which takes a Vandermonde matrix containing shapes similar to the DFT matrix. In contrast, the strength of the spatial mode at the dominant frequency decreases with a factor of $1/\sqrt{A}$ times as well as to the length of the time-series data. The results, corrected by scaling factors, show a consistent amplitude and spatial mode strength at the dominant frequency regardless of the data lengths. The same results are obtained for two-dimensional artificial signal field data.

Second, the effects of spatial resolution on the DMD amplitudes and spatial mode strengths are investigated using two-dimensional IBPM vortex shedding simulation data. The results show that the spatial data size affects both the amplitudes and the strengths of the spatial modes. With increasing spatial resolutions, the overall amplitude increases proportionally. Regarding spatial modes, a decreasing tendency is observed in all spatial modes as the spatial resolution increases. The results corrected by the scaling factors show good agreements again, regardless of changing spatial resolutions. Only slight errors are observed at the lowest spatial resolution.

Finally, the effects of spatial resolution and the correction of both DMD amplitudes and spatial mode strengths using PIV data of a laminar pulsating jet are investigated. Four interrogation window conditions are used. As a result of the DMD analysis, only the dominant mode and the first harmonics are confirmed. The DMD amplitude and spatial mode strength, which are also affected by the spatial resolution of the spatial data size, show the same trend as those obtained with numerical results. Using the proposed scaling factor, an interpretation excluding the effect of the spatial resolution of the data is possible.

Therefore, it can be concluded that a quantitative flow field analysis of the DMD based on a mathematical approach is proposed. Quantitative analysis of fluid flow using DMD allows for consistent results across various types of flow analysis and enables comparisons among different analysis methods

for fluid flow.

Building upon these findings, further analysis beyond the scope of this article will include a quantitative analysis of velocity measurement techniques for fluid flow and how external factors, such as the effects of noises, analysis methods, and interrogation windows, affect the amplitude and spatial modes of DMD. Additionally, this will encompass quantitative analysis and error assessment based on analysis techniques in 1D and 2D velocity analysis tools like Optical Flow, not limited to PIV, and include noise analysis.

CRediT authorship contribution statement

Jeonghoon Lee: Conceptualization, Methodology, Visualization, Writing-Original draft preparation, Investigation, **Takeshi Saito**: Reviewing & Editing, **Shinji Nakaya**: Reviewing & Editing, **Mitsuhiro Tsue**: Reviewing & Editing, **Laurent Zimmer**: Conceptualization, Design of experiments, Software, Supervision, Data curation, Review & Editing

Declarations

The authors declare that they have no known competing financial interests or personal relationships that could have appeared to influence the work reported in this paper.

Data availability

Data will be made available on request.

Declaration of interests

No funding was received for this work

Acknowledgments

None

References

[1] B. Van Oudheusden, Piv-based pressure measurement, Measurement Science and Technology 24 (3) (2013) 032001.

[2] R. Ainsworth, R. Miller, R. Moss, S. Thorpe, Unsteady pressure measurement, Measurement Science and Technology 11 (7) (2000) 1055.

[3] C. E. Willert, M. Gharib, Digital particle image velocimetry, Experiments in fluids 10 (4) (1991) 181–193.

[4] C. Gendrich, M. Koochesfahani, A spatial correlation technique for estimating velocity fields using molecular tagging velocimetry (mtv), Experiments in Fluids 22 (1) (1996) 67–77.

[5] T. Liu, L. Shen, Fluid flow and optical flow, Journal of Fluid Mechanics 614 (2008) 253–291.

[6] F. Scarano, Iterative image deformation methods in piv, Measurement science and technology 13 (1) (2001) R1.

[7] H. Koizumi, S. Tsutsumi, T. Haga, Sparsity-promoting dynamic mode decomposition analysis on aeroacoustics of a clustered supersonic jet, in: 23rd AIAA computational fluid dynamics conference, 2017, p. 3798.

[8] G. Comte-Bellot, Hot-wire anemometry, Annual review of fluid mechanics 8 (1) (1976) 209–231.

[9] D. Bradley, K. Matthews, Measurement of high gas temperatures with fine wire thermocouples, Journal of Mechanical Engineering Science 10 (4) (1968) 299–305.

[10] S. Nakaya, T. Funahashi, Y. Asakami, I. Fujio, S. Takahashi, M. Tsue, Thermometry of combustion gas measuring two-band near-infrared emissions less than 1.1 μm from water molecules, Experimental Thermal and Fluid Science 94 (2018) 1–8.

[11] A. Hultqvist, M. Christensen, B. Johansson, A. Franke, M. Richter, M. Aldén, A study of the homogeneous charge compression ignition combustion process by chemiluminescence imaging, SAE transactions (1999) 2114–2127.

[12] J. Kojima, Y. Ikeda, T. Nakajima, Spatially resolved measurement of oh*, ch*, and c2* chemiluminescence in the reaction zone of laminar methane/air premixed flames, Proceedings of the Combustion institute 28 (2) (2000) 1757–1764.

[13] V. Nori, J. Seitzman, Evaluation of chemiluminescence as a combustion diagnostic under varying operating conditions, in: 46th AIAA Aerospace Sciences Meeting and Exhibit, 2008, p. 953.

[14] K. R. Rao, D. N. Kim, J. J. Hwang, Fast Fourier transform: algorithms and applications, Vol. 32, Springer, 2010.

[15] P. J. Schmid, Dynamic mode decomposition and its variants, Annual Review of Fluid Mechanics 54 (2022) 225–254.

[16] C. W. Rowley, I. Mezić, S. Bagheri, P. Schlatter, D. S. Henningson, Spectral analysis of nonlinear flows, Journal of fluid mechanics 641 (2009) 115–127.

[17] I. Mezić, Analysis of fluid flows via spectral properties of the koopman operator, Annual Review of Fluid Mechanics 45 (2013) 357–378.

[18] Y. Susuki, I. Mezic, Nonlinear koopman modes and coherency identification of coupled swing dynamics, IEEE Transactions on Power Systems 26 (4) (2011) 1894–1904.

[19] F. Richecoeur, L. Hakim, A. Renaud, L. Zimmer, Dmd algorithms for experimental data processing in combustion (2012).

[20] T. W. Muld, G. Efraimsson, D. S. Henningson, Flow structures around a high-speed train extracted using proper orthogonal decomposition and dynamic mode decomposition, Computers & Fluids 57 (2012) 87–97.

[21] M. S. Hemati, C. W. Rowley, E. A. Deem, L. N. Cattafesta, De-biasing the dynamic mode decomposition for applied koopman spectral analysis of noisy datasets, Theoretical and Computational Fluid Dynamics 31 (4) (2017) 349–368.

[22] A. T. Mohan, D. V. Gaitonde, Analysis of airfoil stall control using dynamic mode decomposition, Journal of Aircraft 54 (4) (2017) 1508–1520.

[23] J. N. Kutz, S. L. Brunton, B. W. Brunton, J. L. Proctor, Dynamic mode decomposition: data-driven modeling of complex systems, SIAM, 2016.

[24] M. R. Jovanović, P. J. Schmid, J. W. Nichols, Sparsity-promoting dynamic mode decomposition, Physics of Fluids 26 (2) (2014) 024103.

[25] P. J. Schmid, Dynamic mode decomposition of numerical and experimental data, Journal of fluid mechanics 656 (2010) 5–28.

[26] W. Pijnappel, A. Van den Boogaart, R. De Beer, D. Van Ormondt, Svd-based quantification of magnetic resonance signals, Journal of Magnetic Resonance (1969) 97 (1) (1992) 122–134.

[27] J. Jensen, S. H. Jensen, E. Hansen, Exponential sinusoidal modeling of transitional speech segments, in: 1999 IEEE International Conference on Acoustics, Speech, and Signal Processing. Proceedings. ICASSP99 (Cat. No. 99CH36258), Vol. 1, IEEE, 1999, pp. 473–476.

[28] J. Ying, J.-F. Cai, D. Guo, G. Tang, Z. Chen, X. Qu, Vandermonde factorization of hankel matrix for complex exponential signal recovery—application in fast nmr spectroscopy, IEEE Transactions on Signal Processing 66 (21) (2018) 5520–5533.

[29] M. Kuian, L. Reichel, S. Shiyanovskii, Optimally conditioned vandermonde-like matrices, SIAM Journal on Matrix Analysis and Applications 40 (4) (2019) 1399–1424.

[30] J. H. Tu, Dynamic mode decomposition: Theory and applications, Ph.D. thesis, Princeton University (2013).

[31] J. H. Tu, C. W. Rowley, D. M. Luchtenburg, S. L. Brunton, J. N. Kutz, On dynamic mode decomposition: Theory and applications, Journal of Computational Dynamics 1 (2) (2014) 391–421. doi:10.3934/jcd.2014.1.391.
URL `/article/id/1dfebc20-876d-4da7-8034-7cd3c7ae1161`

[32] T. Colonius, K. Taira, A fast immersed boundary method using a nullspace approach and multi-domain far-field boundary conditions, Computer Methods in Applied Mechanics and Engineering 197 (25-28) (2008) 2131–2146.

[33] C. H. K. Williamson, Vortex dynamics in the cylinder wake, Annual Review of Fluid Mechanics 28 (1) (1996) 477–539. doi:10.1146/annurev.fl.28.010196.002401.

[34] R. Courant, K. Friedrichs, H. Lewy, On the partial difference equations of mathematical physics, IBM journal of Research and Development 11 (2) (1967) 215–234.

[35] M. S. Hemati, M. O. Williams, C. W. Rowley, Dynamic mode decomposition for large and streaming datasets, Physics of Fluids 26 (11) (2014) 111701.

[36] B. R. Noack, W. Stankiewicz, M. Morzyński, P. J. Schmid, Recursive dynamic mode decomposition of transient and post-transient wake flows, Journal of Fluid Mechanics 809 (2016) 843–872.

[37] D. Durox, S. Ducruix, F. Lacas, Flow seeding with an air nebulizer, Experiments in Fluids 27 (5) (1999) 408–413.